A Novel Instrument for Real-Time Measurement of Attenuation of Weather Radar Radome Including Its Outer Surface. Part II: Applications

Alessio Mancini, Jorge L. Salazar, Rodrigo M. Lebrón, and Boon Leng Cheong

School of Electrical and Computer Engineering, and Advanced Radar Research Center,
University of Oklahoma, Norman, Oklahoma.

ABSTRACT

The concept and theory of a novel instrument to characterize the radio frequency performance of a radome under different conditions, including dirtiness, wetness, and varying temperature, was presented and discussed in Part I. The proposed concept estimates the transmittance through the radome using the reflected signal, directly measured, and an algorithm to evaluate the water absorption on the radome surface. In this second part of the paper, the proposed concept was employed to characterize the radome of an operative X-band weather radar in both dry and wet conditions.

1. Introduction

Among the factors that contribute to bias radar operation, the condition of the radome is the most critical one. In fact, the presence of the radome impacts measurement precision, especially in wet conditions. An accumulation of water can be identified as water film, droplets, or rivulets. The form of water varies as a function of the geometry of the radome and its outer surface condition. The characterization of the influence of the water over the radome was extensively discussed in Salazar-Cerreno et al. (2014), Mancini et al. (2017), and Mancini et al. (2018, hereinafter Part I).

Part I proposed a new instrument to evaluate, in real time, the effect of a wet radome on radar performance as a result of the reflection coefficient measurement at the air–radome interface. The instrument operates using a single-port reflectometer connected to a probe, and it employs the time domain gating (TDG) analysis to improve the measurement quality. Since the radome characterization is based on the reflection coefficient (or reflectance) measured by the reflectometer, an analytical model of a wet radome was created to evaluate the level of absorption of water, either as a slab or as droplets at different rain rates. Numerical simulations performed in Ansys High-Frequency Structural Simulator (HFSS) confirmed the validity of the analytical model and showed that water absorption is not

negligible. Once the absorption quantity is calculated, the transmittance through a wet radome can be estimated. Work presented in Part I concluded with laboratory measurements using a suitably designed setup. Results showed that TDG is a necessary analysis to improve measurement accuracy.

In this second part of the paper, we present an application of the method to a bullet-shaped radome of the PX-1000 (Cheong et al. 2013) to validate the proposed method. The PX-1000 is an operative dual-polarized weather radar, developed by the Advanced Radar Research Center at the University of Oklahoma. The algorithm to perform the correction of a wet radome presented in Part I is here applied to the experiment of natural rain, described later, to estimate water absorption. For the field experiments, the same vector network analyzer (VNA) reflectometer from Copper Mountain and the same dielectric rod antenna that were discussed in Part I were used. Because the reflector system of the PX-1000 was not available for the tests discussed in this part of the paper, a robot arm placed in the location of the radar pedestal was used. In this way it was still possible to characterize the full geometry of the radome, maintaining the probe orthogonal to the radome and assuring high accuracy of the probe position during the tests.

Section 2 of this paper provides a description of the PX-1000 bullet-shaped radome and detailed information about the measurement criterion. In section 3 the experimental results in terms of reflectance and estimated transmittance are shown. Radio frequency (RF) characterization

Corresponding author: Alessio Mancini, amancini@ou.edu

was performed in dry conditions for the cylindrical base and the hemispherical part of the radome. The hemispherical part was also tested in wet conditions, under both artificial and natural rain. For all scenarios, measurements in the horizontal (H) and vertical (V) planes were performed. A summary and a comparison of the results are shown at the end of section 3. In the appendix, more information about the robotic arm and the software used to execute the experiments is provided.

2. Experimental setup

a. X-band radome

Figure 1 shows photographs of the PX-1000 radome taken outdoors on a sunny day. The physical external dimensions of the bullet-shaped radome are 87.23 in. (2.22 m) in diameter, 75.25 in. (1.91 m) in total height, and 31.63 in. (0.8 m) for the height of the cylindrical base. The dark areas noticeable in most of the panels in Fig. 1 are nonhomogeneities located inside the radome. Such nonhomogeneities are imperfections occurring during either the fabrication or assembly processes, and they can generate nonuniform levels of attenuation in various parts of the radome. An example is visible in Figs. 1a, 1b, and 1c, where a dark area, similar to a horizontal "figure 8," is discernible. Another factor that could introduce an additional level of attenuation is due to the junctions where the panels composing the radome are attached to each other. Radome panelization is noticeable in Fig. 1f. Furthermore, the radome is constructed in halves, with the dark vertical line appearing in the first four photographs in Fig. 1 showing the junctions between them. An additional element that is able to affect dual-polarized radar performance is the geometry of the honeycomb hexagons composing the radome. Honeycomb geometry forms different patterns along the directions of x and y, resulting in the distance between adjacent hexagons being different in the vertical and horizontal directions (red double-headed arrows in Fig. 1e). All of the abovementioned factors may affect the level of polarization in the V and H planes and the related attenuation. This effect is accentuated when water is present on the outer surface of the radome.

Besides the flaws apparent by simple visual inspection, other imperfections might be present that cannot be detected by the naked eye. To detect and quantify the effect resulting from all imperfections, a dry radome RF characterization is useful. Mapping the position of the imperfections makes it possible to correct for attenuation of the radome while the radar is operating.

b. Measurement criteria

Characterization of the bullet-shaped radome was performed using a robotic arm. The hemispherical part of the radome was tested both in dry and wet conditions. The cylindrical part was characterized only in dry conditions because of time limitation. This limitation was a factor only in the natural rain experiment and is discussed below. Dry and wet scenarios were studied considering both polarizations (H and V). However, given that only a single-polarized probe was available, only one polarization at a time was measured. First, a full scan of the radome for one polarization was taken. Successively, the scan for the second polarization was executed. The time span elapsing between the beginning of the measurement associated with the first polarization and the start of the test for the second polarization depends on the angle resolutions in azimuth and elevation of the robotic arm. Radome characterization was performed by scanning 360° in azimuth for each cut in elevation. The range in elevation began from 0° and ended at 80°. The angle resolutions were 1° in azimuth and 5° in elevation. Using such fine angle resolutions to fully characterize the radome, each polarization measurement took approximately 2 h and 30 min (9 min per azimuth scan). The time span for characterizing the radome can be shortened by decreasing the resolution or increasing the speed of the robotic arm rotation. While taking a sample of the reflection coming from the radome, the robot did not move. The robotic arm was rotating in azimuth with a resolution dictated by the user (1°). The arm stopped at the point where the measurement was supposed to be taken and then moved to the next position. Continuous movement of the arm was not possible in order to know the azimuth position of the robot and relate it to the sample taken. This was just a limitation of the LabVIEW code developed by author. In brief, both the noncontinuity of the robot rotation to collect each sample and the angle resolutions contributed to increasing the total time for the radome characterization. In practical applications the dielectric rod antennas (for H and V polarizations) would be mounted on the back of the radar feed, scanning with the speed dictated by the radar. As mentioned in Part I, for operative cases the probe needs to be miniaturized (shortened) to avoid degradation of the radar sidelobes.

The experiments were performed outdoors, applying the TDG analysis with a 3-GHz bandwidth (7–10 GHz). Such a frequency range provides a suitable resolution in the time domain as discussed in Part I. The start and stop times of TDG were set to 5.3 and 6.44 ns, respectively.

The study was performed under wet conditions of both artificial and natural rain. Under artificial precipitation a sprinkler was employed to allow a constant flow of water, with wind being the only variable factor, since the experiment was performed outdoors. To have full radome characterization with the mentioned angle resolutions, a
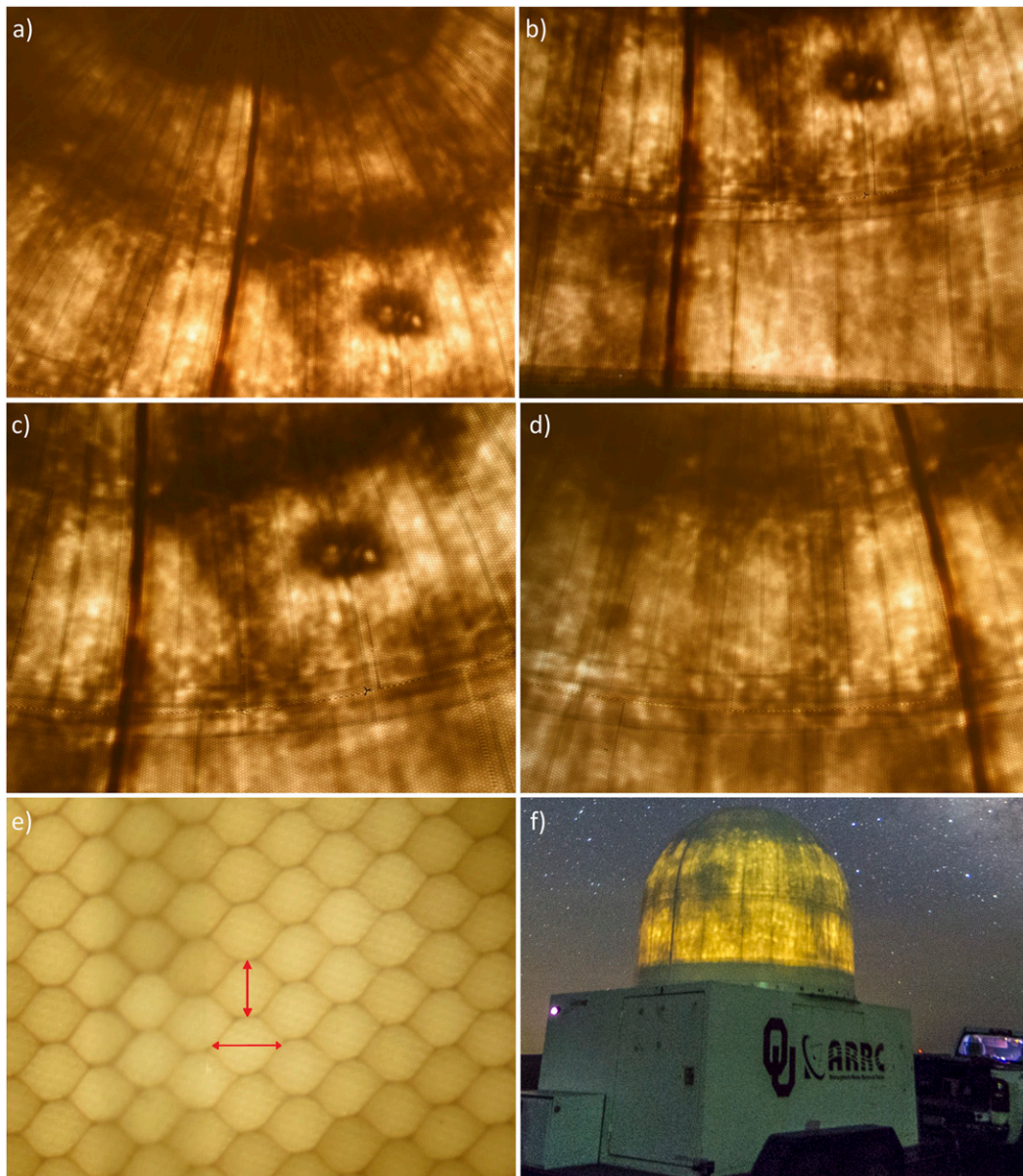
FIG. 1. The PX-1000 radome: (a) an overview, (b) the cylindrical base, and (c),(d) two photographs of the spherical part at different azimuth locations, (e) a close-up, and (f) a long-exposure photograph taken at night (the photograph is provided through the courtesy of J. Kurdzo).

long time span for the execution was required. This was critical for the natural rain scenario, because for the measurement to be completed, the rain had to last long enough. This explains why the cylindrical part of the radome was not considered for investigations performed in wet conditions. In the data collected under natural rain, the storm lasted long enough to characterize the full hemispherical part of the radome. However, the rain rate was not constant during the test, so scans at different elevation angles measured reflections from the radome

under different rain intensities. Varying rainfall also occurred when the two polarizations were measured. All scenarios of the radome characterizations started at the elevation of 0° and concluded at 80°. Starting elevation is important for the natural rain experiment in order to know the related rain rate. A plot of the rain rate will be shown later to provide information about the rainfall at the time of the experiment. In this way it is possible to know the rain rate $[\mathrm{mm}\,(10\,\mathrm{min})^{-1}]$ at the exact moment that an azimuth scan was performed.
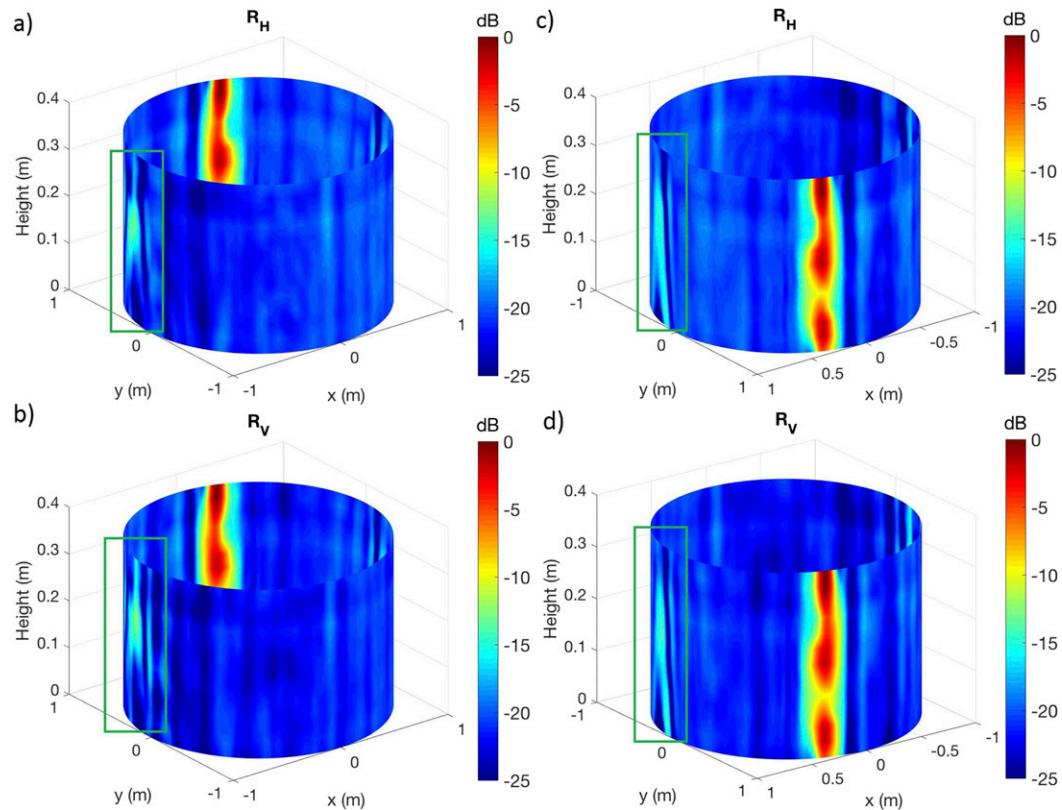
FIG. 2. The R measurement for the cylindrical part of the radome in dry conditions for the (top) H and (bottom) V polarizations for (a),(b) one side and (c),(d) the other side of the radome. The line marked in red represents the reflection coming from the metal strip.

3. Experimental results

The experiments performed for the bullet-shaped radome (Fig. 1) of the PX-1000 weather radar will be discussed in this section.

On one-quarter of the surface of the radome hemisphere, Rain-X was applied before starting the experiment in wet conditions. Rain-X by ITW Global Brands is a substance designed to increase the hydrophobic properties of car windshields to improve visibility, keeping water in droplet form. It is a hydrophobic silicone polymer that forces water to bead and roll off of the car. Rain-X was employed in this experiment to compare different water formations on the surface of the radome. For instance, droplets and rivulets were anticipated to be distributed on the portion of the radome where Rain-X was applied, while a continuous film was expected on the reminder of the radome. The Rain-X-treated portion of the radome is predicted to have a different response than the untreated area in terms of reflectance R and transmittance T. Furthermore, the presence of Rain-X will have a different influence when the signal is horizontally polarized than when it is vertically polarized. This is not expected on

the rest of the radome where water distributes as a continuous film.

For the dry scenario, the cylindrical and hemispherical parts of the radome will be discussed separately. The scenario for the wet case will be presented showing the characterization of the radome for only the hemispherical portion. The results for each of the cases will be discussed, presenting the reflectance and the estimated transmittance for H and V polarizations (R_H, T_H and R_V, T_V, respectively). The absorption of the radome in dry conditions was neglected for reasons addressed in Part I, and that for the wet radome is estimated by using the algorithm discussed in Part I. A vertical metal strip, of 15.6 cm width, was placed on the outer surface of the radome to provide a reference during the tests.

a. Case 1: Cylindrical radome in dry conditions

The cylinder was tested only in dry conditions. The related measurements are shown in Fig. 2 for the reflectance and Fig. 3 for the transmittance. In all the panels of Fig. 2, it is important to note the area of high reflection discernible on the left side of the radome. The level of reflectance at that location is about −12
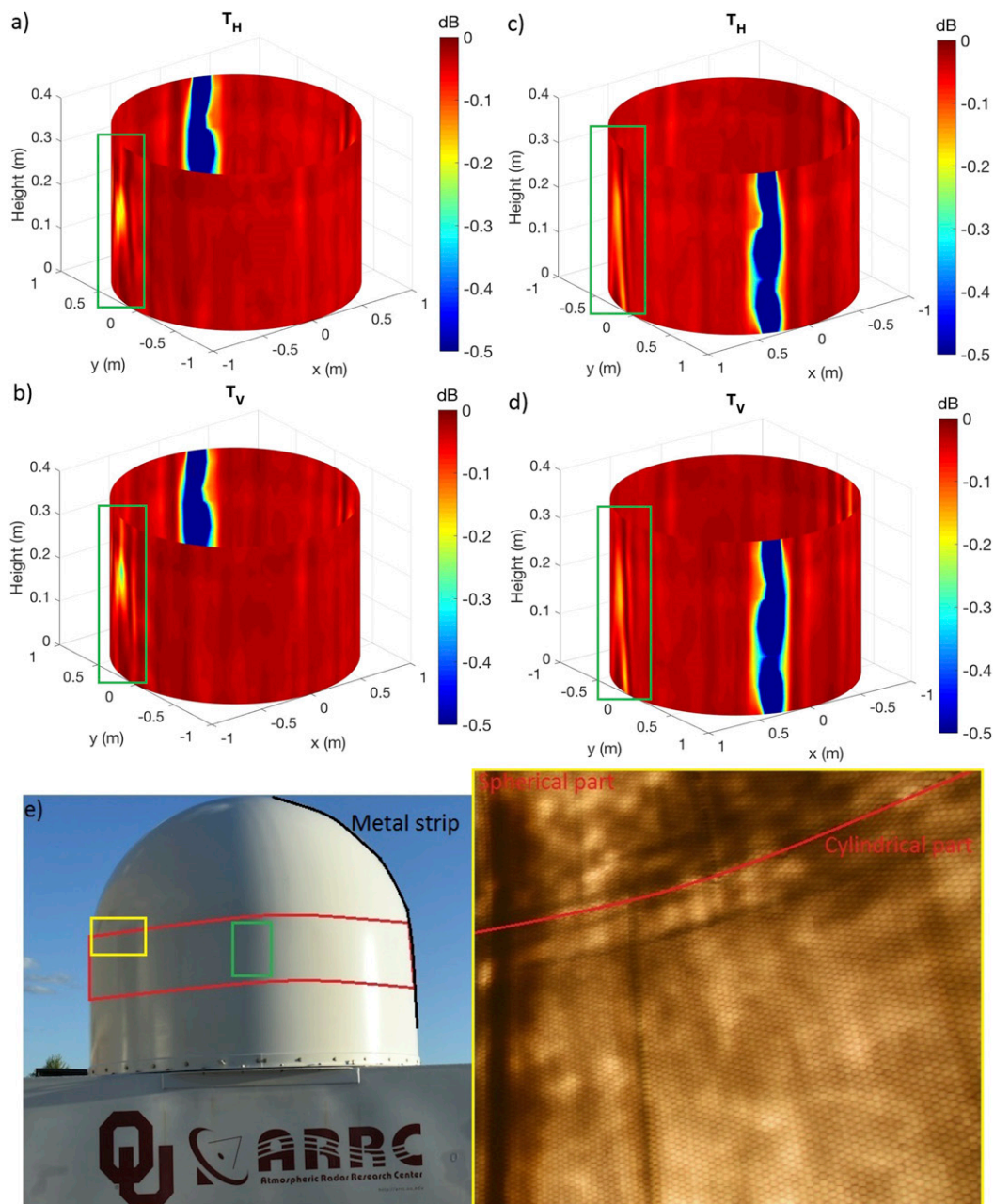
FIG. 3. As in Fig. 2, but for *T*, neglecting the absorption. (e) Photographs of (left) the radome from outside and (right) a close-up of the internal view.

and −17 dB on the two sides of the radome. This area of high reflection is probably due to an imperfection produced during the assembly process. The cylindrical part of the radome is constructed with joined halves. The area shown in this figure is the junction where the two halves are attached and patched, introducing a discontinuity. When the probe scans in the regions where such imperfections occur, diffraction is generated. In the rest of the cylindrical part of the radome, the level of the

reflectance is about −25 dB, in agreement with the simulation performed in Fig. 1 in Part I.

The transmittance for the test performed under dry conditions is shown in Fig. 3. The two polarizations present similar values of the transmission coefficient (~−0.1 dB). This value also matches the magnitude of the transmission coefficient presented in Fig. 1 in Part I. To the left of these figures, corresponding to the spot where the radome imperfection is located, an area with
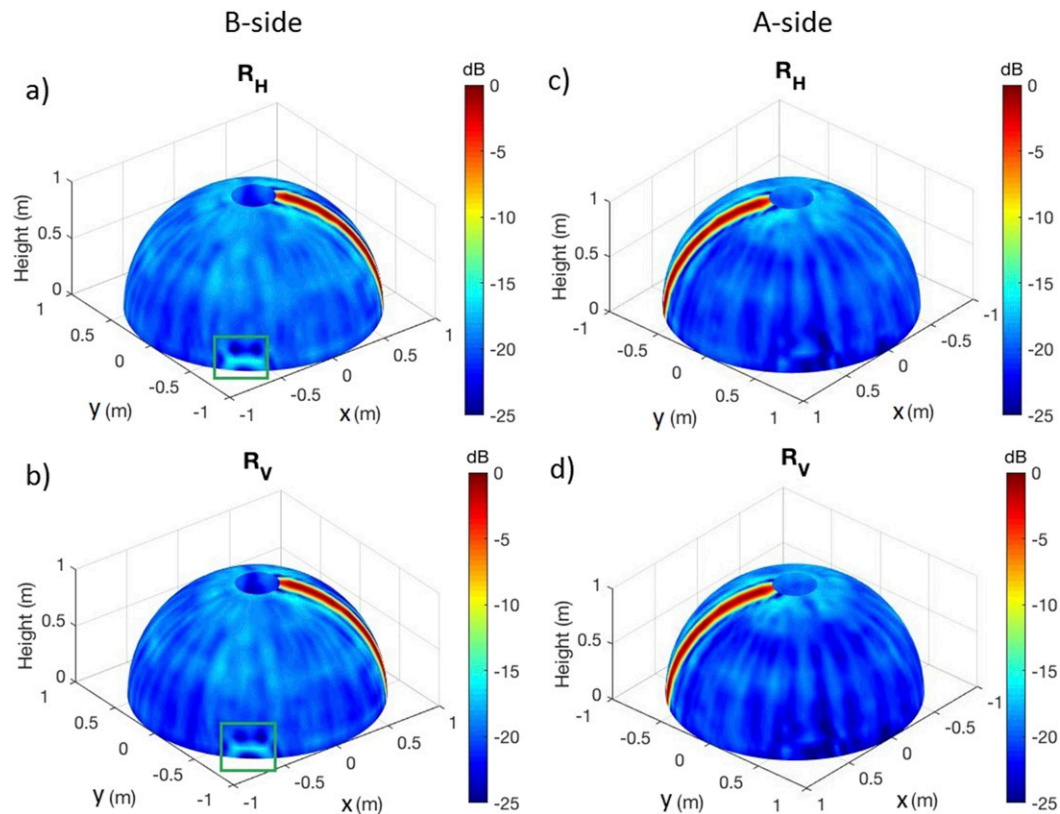
FIG. 4. As in Fig. 2, but for the hemispherical part.

0.2-dB attenuation is noticeable. This flaw generates a peak of −0.25 dB when the probe is vertically polarized (Fig. 3b). This peak value is not reached when the probe is horizontally polarized (Fig. 3a), suggesting that the imperfection affects the two polarizations in a slightly different way, probably because of the geometry of the flaw. In Fig. 3e a photograph of the radome from outside and a close-up of the inside are shown. Highlighted in Fig. 3e are the characterized portion of the cylinder (red), the locations where the internal close-up was taken (yellow), and the flaw in the radome (green).

b. Case 2: Semispherical radome in dry conditions

Reflectance results for the hemispherical part of the bullet-shaped radome are shown in Fig. 4. Just as with the cylindrical portion, the spherical part of the radome shows good agreement between both polarizations. Looking at Figs. 4a and 4b for R, or equivalently at Figs. 5a and 5b for T, another example of a flaw not detectable by visual inspection is located at the base of the hemisphere, but it is present only on the B side of the radome. The flaw is shown in Figs. 4a and 4b in a green frame. In the authors' opinion, this is an air gap formed during the assembly of the radome. The level of higher reflection that is generated by diffraction occurring at the border of the air gap is due to manufacturing imprecision. There is also some difference in the order of magnitude between the A and B sides (Fig. 4). On the B side, vertical lines showing a reflection coefficient of −17 dB are more frequent than on the A side, for both polarizations. A magnitude of −25 dB is more uniformly distributed on the A side, in agreement with the value of reflectance found in Fig. 1 in Part I. In Fig. 5, the transmittance is shown. Similar comments can be deduced for T. A photograph of the external part of the radome is shown in Fig. 5e, where the portion of the radome characterized is highlighted by a red line and the spot related to the imperfection is marked in green. Two close-ups of the internal part of the radome, taken at different elevations, are also shown.

c. Case 3: Semispherical radome under artificial rain

A common garden sprinkler was employed to produce artificial rain. No rain rate or drop size distribution (DSD) was taken into account when wetting the radome. As a result of the consistent flow of water through the sprinkler, the artificial rain was fairly uniform over time, except for the impact of wind. The purpose of this test was to evaluate the effect of a continuous intense rain over the radome. In Fig. 6, a photograph shows the rain setup used
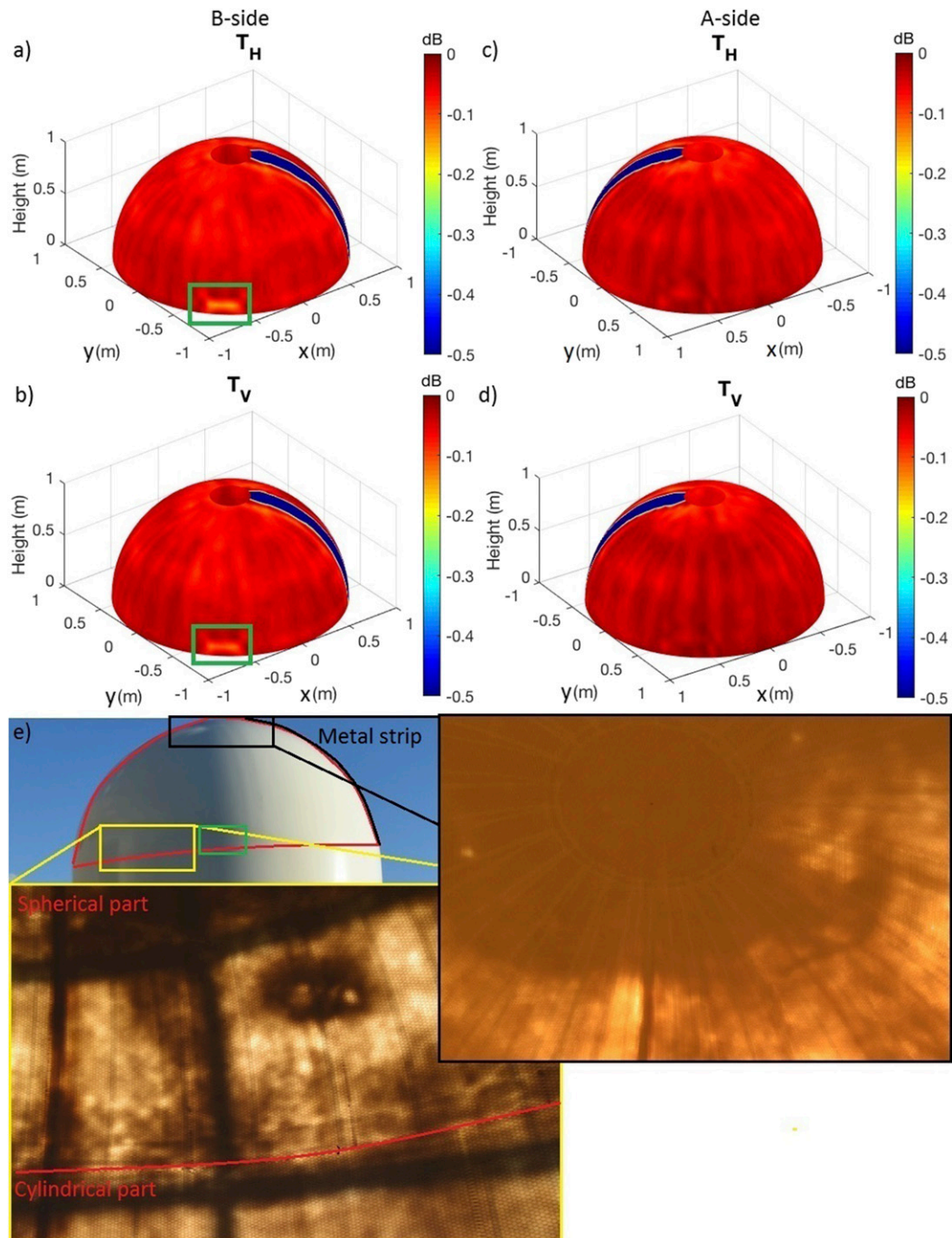
FIG. 5. The *T*, neglecting the absorption, for the spherical part of the radome in dry conditions for the (top) H and (middle) V polarizations for (a),(b) the B side and (c),(d) the A side of the radome. (e) Photographs of the radome from outside and two close-ups of the internal view.

for this experiment. The setup was designed with the sprinkler pointing at the top of the radome so that the water stream could flow down naturally and equally on both sides. The schematic representation depicted at the top-right corner in Fig. 6 shows a top view of the radome

and the related sector subdivisions called A and B sides. The B side directly faces the sprinkler. Although the water flow was supposed to hit the radome from the top, wind action caused uneven water distribution on the radome. As a consequence of the wind, it was predicted that
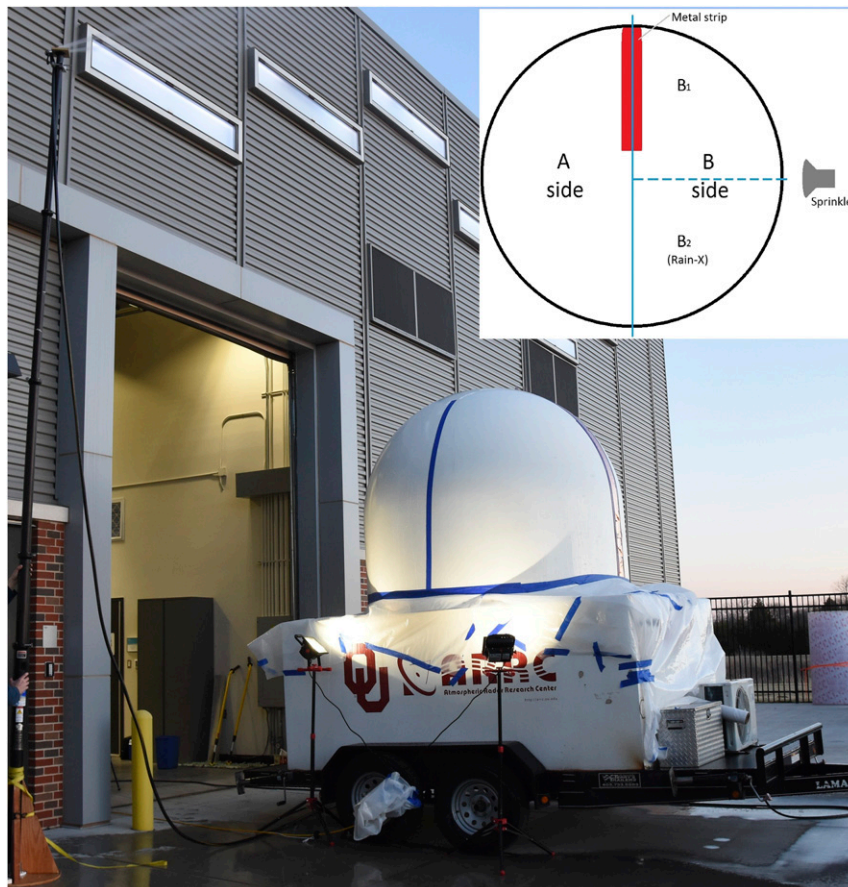
FIG. 6. A photograph taken during the radome characterization under artificial rain. (top right)
A schematic representation (top view) of the radome subdivision (not to scale).

the A side would be less exposed to the rain than the B side. The B_2 side, a subsection of B, is the sector where Rain-X was applied.

The following test under artificial rain conditions was performed on 25 February 2016, the same day that Rain-X was applied to the radome. A comparison between the A side and the B_2 sector is shown in Fig. 7. The photographs were taken during the experiment using artificial rain and show a comparison between the part of the radome not treated with Rain-X and the area where it was applied. Only the B_2 sector presents droplets, while on the rest of the radome a water film of varying thicknesses is formed. Different thickness of the water film may occur as a consequence of the wind presence, because one portion of the radome might not be exposed to the same rain intensity as another part. However, in this case, the ''wavy'' pattern of the film shown in Fig. 7f is due to the fact that when a critical thickness is reached, water just runs off, producing wavy behavior (Ruze 1965). In the photograph, droplets and rivulets on the B_2 side are highlighted. In

Fig. 7a the Rain-X effect is shown. In the portion of the radome where Rain-X was applied, the water remains as droplets or rivulets, while it stays as a film on the rest of the radome. The photograph in Fig. 7b emphasizes the A side, showing that the water film is not homogeneous but actually appears wavy (close-up in Fig. 7f). The top part of B_2 was not treated with the hydrophobic substance because it was not possible to be physically reached. Consequently, at the top of this sector, the water distributes as a film, like the other untreated areas of the radome. This is confirmed in the close-up in Fig. 7c, where the distinction between the part of the radome where Rain-X was applied and the top portion without Rain-X is obvious. In Figs. 7d and 7f, two close-ups of the B_2 side are shown. In these figures, the droplet and rivulet formations caused by the Rain-X effect are highlighted.

The measured reflectance is shown in Fig. 8. It is immediately obvious the level of reflection increased as a result of the heavy rain (Figs. 8c and 8d). For such an area, the level of reflection rose from -20 dB in dry
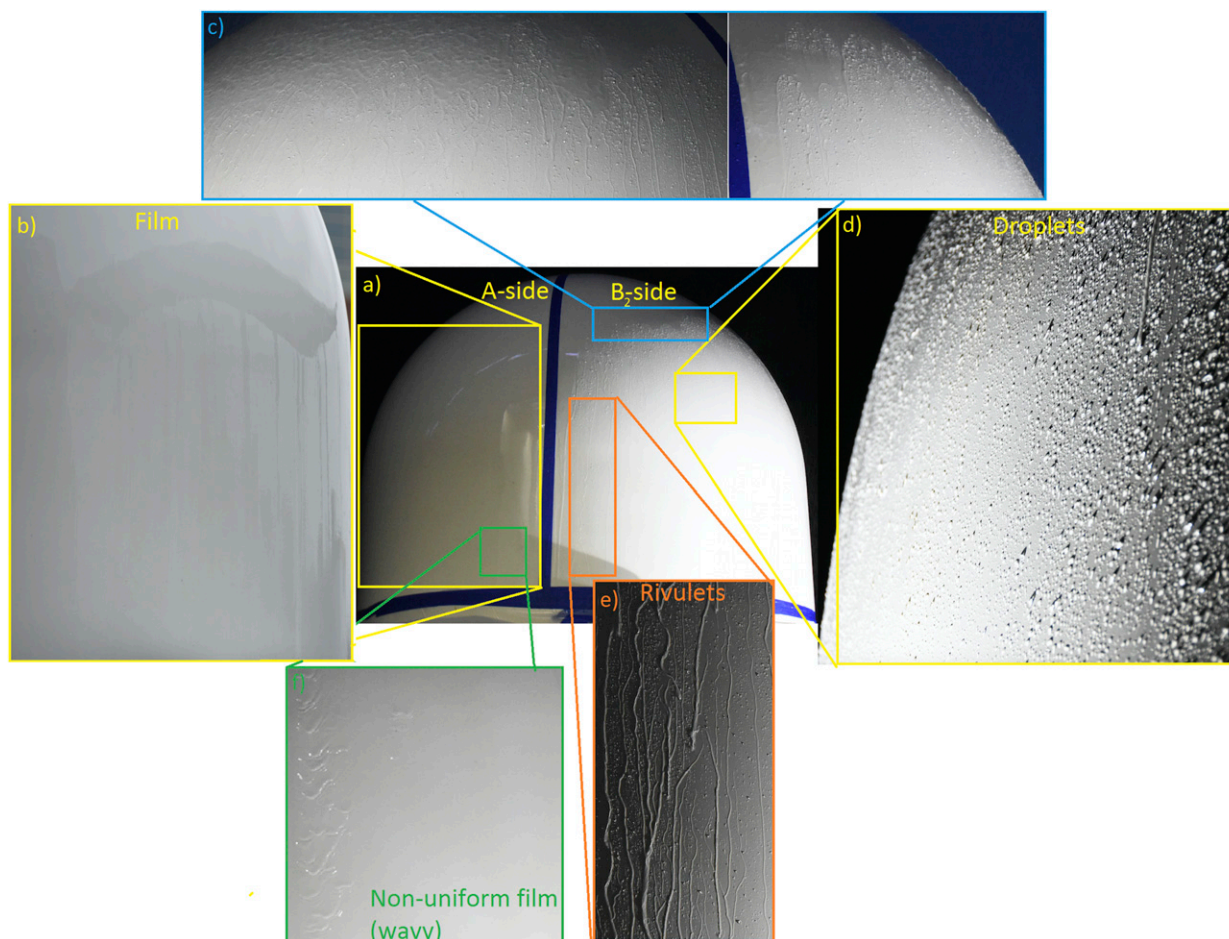
FIG. 7. (a) A photograph that shows the Rain-X effect during artificial rain. A comparison of the water distribution between the (b) A side and (d) B_2 sector are shown in close-ups. (c) The boundary where Rain-X was applied. Close-ups of the (f) A and (e) B_2 sides show the continuous but nonhomogeneous film and the rivulet formations, respectively.

conditions to -6 dB in wet conditions. Figure 8a presents the reflections for the H polarization for the sector treated with Rain-X (B side). Reflections are lower (below -10 dB) at the bottom of the hemisphere and higher (~ -6 dB) at the top part of the hemisphere, where Rain-X was less efficient. However, the transition from -6- to -15-dB reflectance, visible in Fig. 8a, does not match with the elevation corresponding to the top border where Rain-X was not applied. This value of the transition of the reflectance is probably more due to the large stream of water occurring at the top of the B side, the region where the sprinkler was directly wetting the radome, than it is to exposure to a higher quantity of water (Fig. 6). The hydrophobic effect at that elevation was nullified. There is a noticeable difference between R_H and R_V in the sector treated with the hydrophobic substance. Water stays mostly as droplets and rivulets on hydrophobic surfaces. Rivulets have a vertical geometry, which gives them a larger vertical cross section

than a droplet, while the horizontal cross section is the same as a droplet. This is highlighted in the photographs shown in Fig. 8e. In this way a rivulet reflects more of an electromagnetic wave polarized in the vertical plane than one polarized horizontally. When water presents as a film (nonhydrophobic portion), there is no remarkable difference between H and V polarizations. This is confirmed by the comparison of Figs. 8a and 8b, where the reflectance is higher for R_V than R_H for the B side (which is partly treated with the hydrophobic substance).

The estimated transmittance is not available because no rain rate was measured at the time of the experiment. Furthermore, even if the rain rate was measured, the sprinkler did not wet the radome in a uniform way for the reasons mentioned earlier. This makes the absorption hard to compute, since the water, either as a film or as droplets/rivulets, was highly nonhomogeneous (Figs. 7 and 8e). As a consequence, the authors chose not
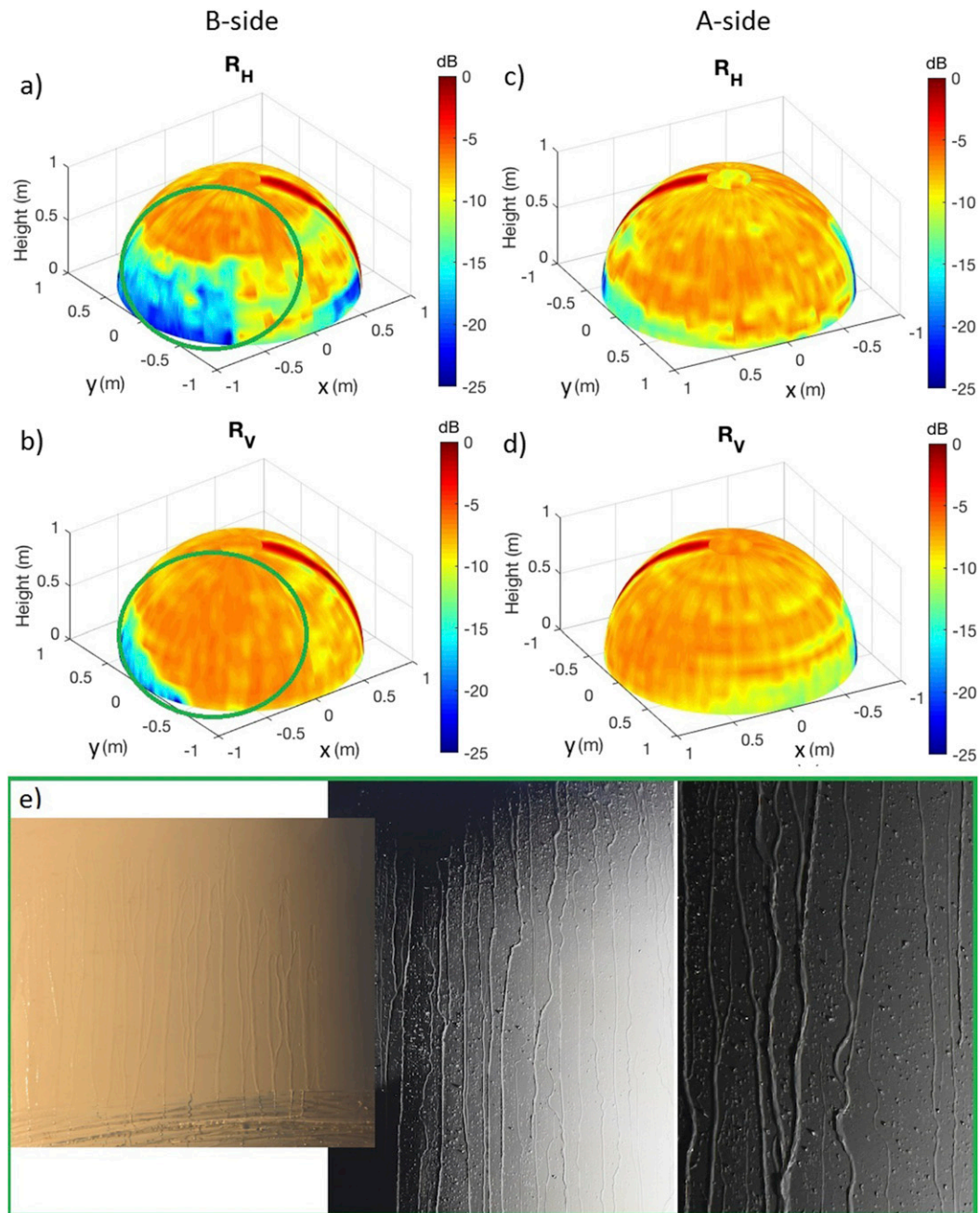
FIG. 8. The R measurement for the spherical part of the radome in wet conditions during artificial rain for the (top) H and (middle) V polarizations for (a),(b) the B side and (c),(d) the A side of the radome. The line marked in red represents the reflection coming from the metal strip. (e) Photographs of rivulet formation occurring on the B_2 side.

to show the transmittance. However, the results of this scenario are still interesting because they highlight the effects of different water formations caused by a very intense stream of water. These two factors show how the level of reflectance was higher than the level of reflection of the dry radome. Various levels of attenuation for the two polarizations are expected, not only in the

sector where Rain-X was applied, but also on the rest of the radome, as Figs. 8c and 8d demonstrate.

d. Case 4: Semispherical radome under natural rain

This test was performed on 17 April 2016, in Norman, Oklahoma. The measurements started at 1910 LT. The rain rate was not uniform across the time span when the
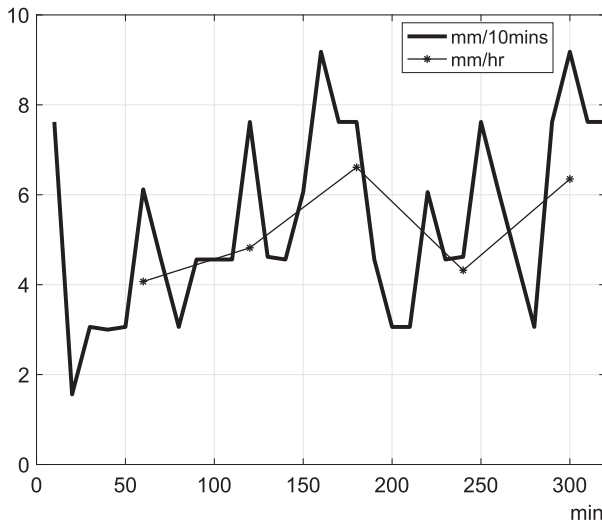
FIG. 9. The average rain rate as a function of time during the storm occurring on 17 Apr 2016. The x axis represents the relative time with respect to the beginning of the measurement. The H polarization was measured first and was started at minute 0. The V polarization was taken immediately after the end of the previous test (at approximately minute 150). The average is calculated every 10 and 60 min. The rain-rate information is provided through a rain gauge from Mesonet (http://www.mesonet.org); the weather station is located within 200 m of the experiment location.

measurements were executed. The radome was first characterized with the probe horizontally polarized and then with the probe vertically polarized. During the time lapse, which lasted from the beginning of the test for the first polarization to the end of the second polarization experiment, different rain rates could have occurred. Figure 9 shows the rain rate averaged every 10 min. Minute 0 in Fig. 9 corresponds to the beginning of the experiment (1910 LT).

The results of the natural rain test are presented in Figs. 10 and 11 for reflectance and estimated transmittance. Although Rain-X was not reapplied for this experiment, its effects were still present from the application in February (Figs. 10a and 10b). In contrast to the test results from the artificial rain, natural rain results were similar for both polarizations for the B_2 side. This is probably because the rain flow was more uniform, and the rain rate was lower than in the case of artificial rain. The Rain-X presence is more accentuated in this scenario as demonstrated in Figs. 10a and 10b. This is in contrast to the results from the other side of the radome (Figs. 10c and 10d). Also, it is noticeable at $\theta \cong 80°$ that the reflectance is higher than at lower elevations. This occurs without distinction among the sectors' subdivisions. In fact, at such elevations the component of the gravity force is smaller than at lower elevations, causing the water to stay more agglomerated and in bigger drops, as discussed

in Salazar-Cerreno et al. (2014). A pattern of horizontal rings is detected on the A side of the radome (Fig. 10), where water distributes as a continuous film. It occurs at various intensities at different polarizations. The rain intensity could have changed during the experiment. However, the pattern of horizontal rings looks consistent and constant in azimuth; therefore, it should not be associated with rain-rate changes.

The estimated transmittance is shown in Fig. 11. Since the rain rates are available every 10 min, as reported in Fig. 9, and the azimuth scan lasted approximately 9 min, it is hard to make a precise correspondence between the azimuth scan and the related rain rate. Therefore, the transmittance was estimated based on the hourly rain rate (the thin line in Fig. 9). It follows that for the H-polarization test, from 0° to 25° elevation, the rain rate of $4 \, \text{mm h}^{-1}$ was used for the correction. From 30° to 60° elevation, $5 \, \text{mm h}^{-1}$ was used to make the correction. A $6.6 \, \text{mm h}^{-1}$ rain rate was used to estimate the absorption from 65° to 80°. For the experiment performed with the probe vertically polarized, which began immediately after the previous experiment (minute 150 in Fig. 9), the rain rate of $6.6 \, \text{mm h}^{-1}$ was used to make the correction in the range 0°–15°. A $4 \, \text{mm h}^{-1}$ rain rate was employed to make the correction in the 20°–45° elevation range. A rain rate of $6.6 \, \text{mm h}^{-1}$ was used to make the correction in the 50°–80° elevation range. In the radome portion shown in Figs. 11a and 11b, the formation of the droplets was considered in estimating the transmittance, while the continuous film formation was used to make the estimation of the transmittance in the remainder of the radome. Procedures to estimate the transmittance of the two different water distributions were discussed in Part I. Two different scales were necessary to represent the transmittance in the two sides of the radome, because the level of absorption was different. Specifically, levels of absorption were higher where the water was distributed as a film than where it was distributed as droplets. The B side of the radome, for both polarizations where droplets and rivulets occurred, is presented in Figs. 11a and 11b. Two photographs, representing the close-ups highlighted on the B side, show the radome condition. Photograph 1 is the transition between the Rain-X portion and the part where the hydrophobic substance was not applied. Photograph 2 shows droplets and rivulets distributed on the B_2 side. Figures 11c and 11d present the A side, where water was distributed as a continuous film. Because the level of absorption was higher on the A side than on the B_2 sector, the level of transmittance was lower and a different scale had to be used. Regarding the A side (Fig. 11c), the order of magnitude of transmittance is very close to the one estimated through simulation in Fig. 7 in Part I, for the
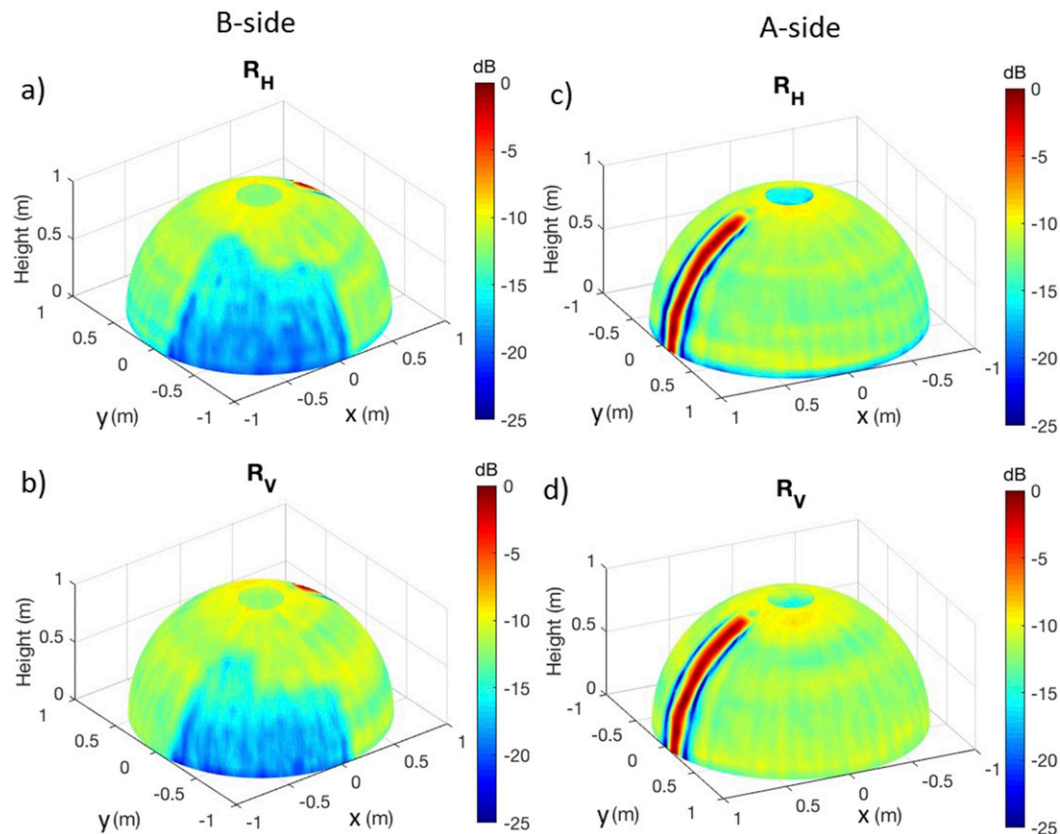
FIG. 10. As in Fig. 8, but in wet conditions during natural rain.

5.3 mm h^{-1} rain rate, where a -2-dB transmittance was obtained. The difference in estimated transmittance between Part I and this part of the paper is probably due to the fact that in the real case, the water formation was affected by wind presence and the dirty conditions of the radome. These factors were not taken into account in the simulation. Furthermore, the vertical lines introduced in Figs. 4 and 5 are still present under natural rain (Figs. 10 and 11). Those lines, the nature of which is unknown to the authors, were not taken into account in the simulation, and they also are the cause of the mismatch with the results of the simulations performed in Part I. The abovementioned vertical lines are also present in the artificial rain results (Fig. 8), but they are less visible (almost hidden) probably because the thicker film of water occurred in that scenario.

e. Summary of the results

This second part of the paper provides a comparison of the measurements obtained for the dry, natural, and artificial scenarios. The results of the experiments were overlapped for different elevation cuts (0°, 30°, and 60°) to better understand the effect of water in different forms over the radome. The rain rate of the artificial rain

was not measured. However, it can be empirically stated that the artificial rain rate was higher than the natural rain rate of the storm that occurred during the experiments for this paper. The purpose of comparing these three scenarios is to have an approximated time series of radome conditions under different rain intensities. The artificial rain case represents conditions of heavy rain, while the natural rain measurement is halfway between wet and dry conditions, since the rain was not particularly heavy the day of the test (17 April 2016). In Fig. 12, the curves of the measured reflection coefficient are overlapped for H and V polarizations. The peak visible in all the curves is due to the metal strip used as the reference. For the dry conditions, the H and V polarizations show similar levels of reflection at all elevations. However, the curve measured with the probe vertically polarized seems to be slightly lower in intensity. This is probably due to the radome composition as shown in Fig. 1e. In the figure, the distribution of hexagons is different along the x and y directions. When the probe is horizontally polarized, the electric field is aligned parallel to the x axis of Fig. 1e. When it is vertically polarized, the field is aligned to the y axis. The distribution of hexagons in the two directions generates different
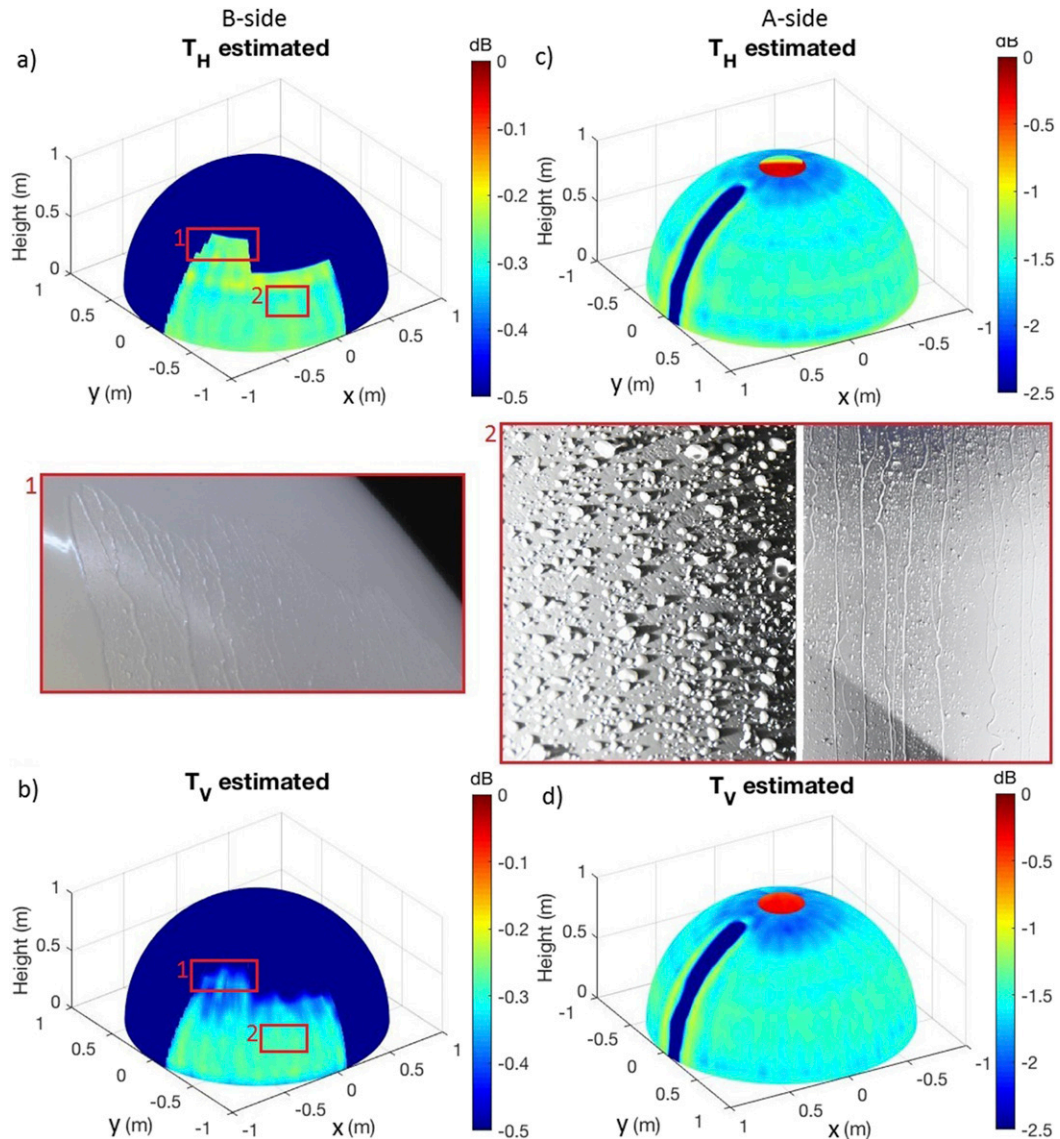
FIG. 11. The T for the hemispherical part of the radome in wet conditions during natural rain for the (top) H and (bottom) V polarizations for (a),(b) the B side and (c),(d) the A side of the radome. (middle) Photographs of the positions identified by the red rectangles in (a) and (b) highlight the (left) rivulets and (right) droplets.

reflection responses in the two cases. In the rain scenarios, however, a higher reflection is measured in the V plane than the H plane. The plot at $\theta = 0°$ has the largest discrepancy between the two polarizations during rain conditions. This is due to the rivulet formation that affects the reflections in the V plane more than in the H plane. In the hydrophobic sector, the reflection coefficient shows peaks of value lower than those that occur in dry conditions. This occurs because scattering from the droplets or rivulets are combined destructively, causing the probe to perceive a lower value of signal. At $\theta = 30°$, a remarkable difference between the two

polarizations is discernible only in the region where Rain-X was applied, especially for the artificial rain conditions. In all the rest of the radome, similar values between the H and V polarizations are shown. The hydrophobic substance was not applied above 60° elevation because of the difficulty in accessing that part of the radome.

The values found in the experiments in this part of the paper were similar to the ones obtained via simulation in Part I. The differences between the numerical and experimental results are probably due to factors such as wind and the actual outer skin conditions of the
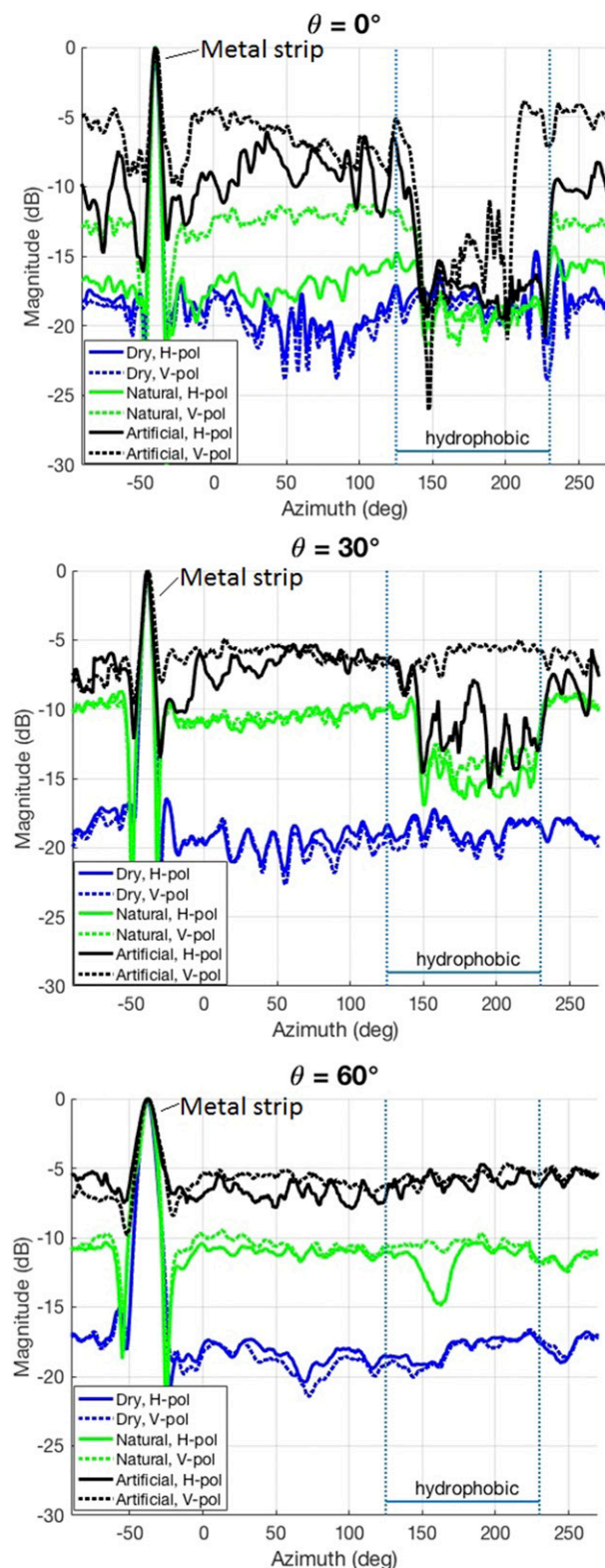
FIG. 12. A comparison of R for the three tested scenarios (dry, natural rain, and artificial rain) for different elevation cuts and both polarizations.

radome that were not considered in the simulation. These factors are complicated to model. Another reason for the discrepancy between theory and measurements is the radome structure. The vertical line pattern occurring in the radome provides nonhomogeneous measurements of reflectance and therefore estimated transmittance. In Part I, a flawless radome was considered for the study. To conclude, Table 1 compares the transmission loss found in the literature with the one computed in this paper. The type of water formation for the experimental cases reported in the literature was not available. However, good agreement is acknowledged between the transmission loss found in this paper with the one measured by Frasier et al. (2013) for the 6.6 mm h^{-1} rain rate. Frasier obtained a 2.2-dB attenuation for the wet radome as compared with the 1.8-dB attenuation found here when water is distributed as a film. In addition, when the rain rate is 6.6 mm h^{-1} for the water film formation, it has the same transmission loss obtained by Chang (1985) at a rain rate of 4 mm h^{-1}. Discrepancies between the attenuation computed in this paper with others available in the literature are probably due to differences in the radome condition, the wind presence (not mentioned in the references), and the temperature of the water. Differences in the results can also be caused by the elevation at which the transmission loss of the wet radome is computed. Although different rain rates occurred during the experiment presented in this paper, water at various elevation angles is subject to a different component of the gravity force, affecting the water accumulation. Furthermore, the last factor that may create differences is that the correction algorithm employed is approximated with the hourly rain rate rather than the actual one measured at each azimuth scan. All these factors make a proper comparison hard to perform.

4. Conclusions

A novel instrument designed to characterize the effect of a wet radome and the related proof of concept was discussed in Part I of this paper. In this second part, the results of tests using the proposed technique employed to characterize the X-band radome of the PX-1000 were discussed. Characterization of the radome under dry conditions maps imperfections caused by the fabrication and assembly processes. Such flaws generate different responses in terms of reflectance and transmittance in the various locations of the radome. The attenuation produced by water was estimated as shown in Part I. In this second part of the paper, it was demonstrated that water presents in different forms on various locations of the radome and

TABLE 1. A comparison between the method proposed in this paper and results presented in the literature relating to transmission from a wet radome for different rain rates and water formations.

Reference	Frequency (GHz)	Approach	Water formation	Rain rate (mm h^{-1})	Transmission loss (dB)
Ruze (1965)	15.5	Analytical	Film	2.8	3.2
Chang (1985)	12	Analytical	Film	4	1.8
Fenn (1997)	19.5	Experimental	—	6	1
Kurri and Huuskonen (2008)	5.65	Analytical	Film	5	1.25
Trabal et al. (2008)	9.375	Experimental	—	5	0.6
Bechini et al. (2010)	9.375	Empirical	Film	4	2.3
				5	2.5
				6.6	2.8
Frasier et al. (2013)	9.4	Experimental	—	4	1.8
				5	2
				6.6	2.2
Salazar-Cerreno et al. (2014)	10	Analytical	Droplets	5	0.15
				10	0.2
			Film	1	0.8
				10	1.8
Mancini et al.	9.55	Analytical	Droplets	4	0.25
				5	0.25
			Film	4	1.3
				5	1.5
				6.6	1.8

changes distribution in time as the rain rate changes. Results for the wet radome executed under artificial rain show different responses for H and V polarizations in the sector where Rain-X was applied. In particular, during the test for the V polarization, the hydrophobic substance did not seem to have any effect, probably because of the larger amount of water that presented as rivulets. For the H polarization, Rain-X clearly lowered the level of reflections because rivulets affect the V plane more than the H plane. By contrast, under natural rain, both the H and V polarizations showed a lower level of reflection in the area where Rain-X was employed. This happens because the rain rate of the natural storm was not as intense as the artificial rain generated by the sprinkler. This highlights how challenging it is to characterize a radome, since many factors influence the process. Imperfections and damages do not influence water formation, but they still affect the radar signal in the location of the scan.

In real scenarios the rain rate is more homogeneously distributed and usually not as intense as in the artificial rain case, and if the surface of the radome is hydrophobic, then water will present as droplets and rivulets over the entire radome surface. If no hydrophobic substance is applied, then water forms as a continuous film over the radome. The estimation of the transmittance is easier to perform for the scenario where water presents as a film than the case where it distributes as droplets and rivulets. Droplets and rivulets produce a lower level of transmission loss than the continuous film of water, but their attenuation is different in the H and V planes. Therefore, it is not convenient to have rivulets form for dual-polarized applications. Results presented in this second part also provide an idea of how much water formation can bias the dual-polarized products. Although the proposed method does not furnish a direct estimation of quantities such as Z_{DR}, it is still able to detect and quantify the different water formations in the various parts of the radome.

Water distribution is also influenced by the component of the gravity force, which is different at various elevation angles of the radome (maximum at the cylindrical base and minimum at the top of the hemisphere). The component of the gravity force affects the thickness of the water film or rivulet formation at different elevation angles of the radome, for the same rain rate. This factor was not taken into account in the correction algorithm, because of the complexity that it would introduce. This is a limitation of the accuracy as a result of the algorithm when it is applied to a radome geometry such as the bullet shape.
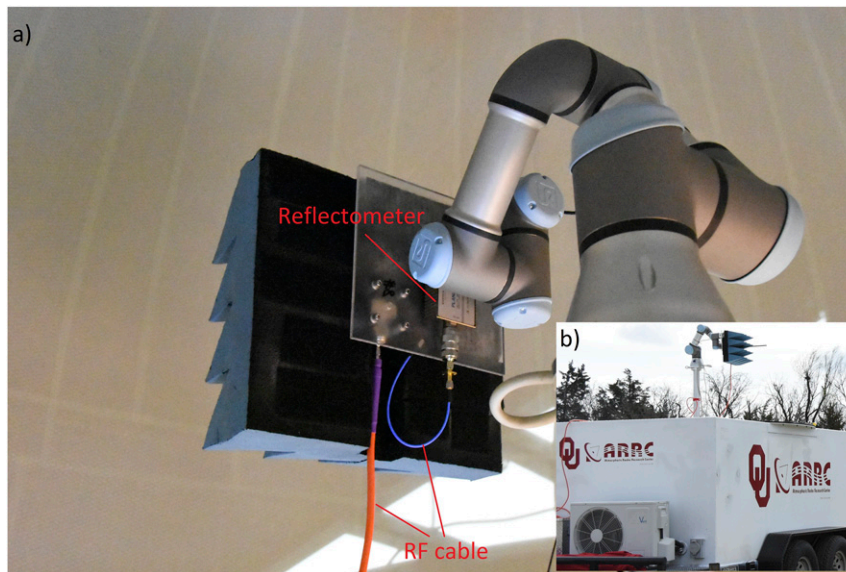
FIG. A1. Two photographs of the robot arm with the probe mounted, taken from (a) the inside with the radome in place and (b) the outside.

APPENDIX

Technical Aspects

a. Robotic arm

Since the radar pedestal was not available at the moment the experiments were performed, a six-axis robotic arm (UR3, Universal Robots) was utilized to replace the PX-1000 pedestal. Since the probe was mounted on the robotic arm, it was possible to allow rotation in azimuth and elevation of the probe while keeping the dielectric rod antenna perpendicular to the area of the radome. The robot is versatile in that it allows for characterization of radomes with different shapes. The robotic arm was programmed to execute movements based on spherical coordinates in agreement with the geometry of the radome to have a full RF characterization both in azimuth and elevation.

The UR3 was positioned in the geometrical center of the radome (location of the radar pedestal) in order to avoid misalignment during the measurements. Moreover, careful mounting ensured correct alignment of the rotation axes of the robot with respect to the radome, in an effort to guarantee an equidistant trajectory between the probe and the inner surface of the radome. In this way, the positioning errors are due to the precision of the robot, which is 0.1 mm, and the inherent manufacturing shape flaws of the radome. In Fig. A1, photographs of the robot arm and the probe fixed on the

robot arm are shown. It is important to emphasize that the robot is used in cases when a radar pedestal is not available. The absorbers placed behind the antenna were employed to limit the reflections coming from the robotic arm. Although TDG was applied during the experiments, reflections from the robot arm should not have altered the tests; a further cautionary measure was desired. Although operational applications would not allow this kind of screening, we demonstrated in Part I that even reflections generated from the closest parts of the setup can be removed by applying TDG.

b. Software interface

A graphic user interface (GUI) was programmed into LabVIEW to create a fully automated system to coordinate the robot movements and the reflectometer. The connection between the laptop and the robot was a wireless Ethernet, and a USB cable was used for the laptop and reflectometer communication. Given the bullet-shaped radome, the GUI was programmed to perform scans in spherical coordinates for the top part (sphere) of the radome. The input parameters to set the reflectometer include the bandwidth and the TDG settings (start and stop times). The input parameters for the robot are the start and stop angles in azimuth ϕ and elevation θ, with related step angles that define the resolution in the measurements, and the type of polarization that rotates the robot arm 90° to bring the probe from H to V polarization or vice versa. The data were saved in a spreadsheet file.

REFERENCES

Bechini, R., V. Chandrasekar, R. Cremonini, and S. Lim, 2010: Radome attenuation at X-band radar operations. *Proc. Sixth European Conf. on Radar in Meteorology and Hydrology (ERAD 2010)*, Sibiu, Romania, National Meteorological Administration, P15.1.

Chang, K.-C., 1985: System performance in rain in a radome-enclosed environment. 1985 IEEE Military Communications Conference *(MILCOM '85)*, Vol. 1, IEEE, 293–299, https://doi.org/10.1109/MILCOM.1985.4794978.

Cheong, B. L., R. Kelley, R. D. Palmer, Y. Zhang, M. Yeary, and T. Yu, 2013: PX-1000: A solid-state polarimetric X-band weather radar and time–frequency multiplexed waveform for blind range mitigation. *IEEE Trans. Instrum. Meas.*, **62**, 3064–3072, https://doi.org/10.1109/TIM.2013.2270046.

Fenn, A. J., 1997: Measurements of wet radome transmission loss and depolarization effects in simulated rain at 20 GHz. *Tenth International Conference on Antennas and Propagation*, Vol. 1, IEE Conference Publication Series, No. 436, IET, 474–477.

Frasier, S. J., F. Kabeche, J. F. I. Ventura, H. Al-Sakka, P. Tabary, J. Beck, and O. Bousquet, 2013: In-place estimation of wet radome attenuation at X-band. *J. Atmos. Oceanic Technol.*, **30**, 917–928, https://doi.org/10.1175/JTECH-D-12-00148.1.

Kurri, M., and A. Huuskonen, 2008: Measurements of transmission loss of a radome at different rain intensities. *J. Atmos. Oceanic Technol.*, **25**, 1590–1599, https://doi.org/10.1175/2008JTECHA1056.1.

Mancini, A., J. L. Salazar, R. M. Lebrón, and B. L. Cheong, 2017: A novel technique to characterize the effect of rain over a radome for radar applications. *Proc. 2017 IEEE Radar Conf. (RadarConf)*, Seattle, WA, IEEE, 470–475, https://doi.org/10.1109/RADAR.2017.7944249.

——, ——, ——, and ——, 2018: A novel instrument for real-time measurement of attenuation of weather radar radome including its outer surface. Part I: The concept. *J. Atmos. Oceanic Technol.*, **35**, 953–973, https://doi.org/10.1175/JTECH-D-17-0083.1.

Ruze, J., 1965: More on wet radomes. *IEEE Trans. Antennas Propag.*, **13**, 823–824, https://doi.org/10.1109/TAP.1965.1138492.

Salazar-Cerreno, J. L., V. Chandrasekar, J. M. Trabal, P. Siquera, R. Medina, E. Knapp, and D. J. McLaughlin, 2014: A drop size distribution (DSD)-based model for evaluating the performance of wet radome for dual-polarized radars. *J. Atmos. Oceanic Technol.*, **31**, 2409–2430, https://doi.org/10.1175/JTECH-D-13-00208.1.

Trabal, J. M., I. Zawadski, and D. J. McLaughling, 2008: A method to correct for wet radome attenuation in CASA radars by the use of a contiguous WSR-88D radar. *Proc. Fifth European Conf. on Radar in Meteorology and Hydrology*, Helsinki, Finland, Vaisala, 0287.